Research Article

Journal of Environmental Nanotechnology

Steady-state Engine Evaluation of Nanoparticle-enhanced Renewable Fuel with Fixed-dose Additive Dispersion

Chongkol Sungoum[1], V. Gopinath[2*], Rakesh Varma Kadupu[3], Xianpeng Wang[4], Ratchagaraja Dhairiyasamy[5,6] and Subhav Singh[7]

[1]Department of Engineering and Technology, Shinawatra University, Pathum, Thailand
[2]Department of Agricultural Engineering, Kongunadu College of Engineering and Technology, Trichy, TN, India
[3]Department of Mechanical Engineering, Aditya University, Surampalem, AP, India
[4]International Institute of Management and Business, Pervomaysky, Minsk City, Belarus
[5]Department of Electronics and Communication Engineering, Saveetha School of Engineering, Saveetha University, Chennai, TN, India
[6]Centre for Promotion of Research, Graphic Era (Deemed to be University), Dehradun, UK, India
[7]Centre of Research Impact and Outcome, Chitkara University, Rajpura, PB, India
[8]Department of Research and Development, Lovely Professional University, Phagwara, PB, India
Received: 26.01.2026 Accepted: 02.02.2026 Published: 30.03.2026
*gopinathv@kongunadu.ac.in

ABSTRACT

Compression-ignition engines remain essential for power generation and transportation, and renewable fuels are employed to reduce regulated emissions. A fixed-dose, direct comparison of oxide-conditioned biodiesels from *Calophyllum*, *Nerium*, and Mahuva under identical operating conditions and measurement protocols has not yet been reported. In this work, steady-state BSFC, BTE, exhaust-gas temperature, CO, HC, NO, and smoke emissions of Al_2O_3-, CeO_2-, and TiO_2-conditioned biodiesels were compared with those of diesel. Biodiesels were produced by base-catalyzed transesterification, conditioned with fixed additive and nanoparticle doses, and evaluated at five brake power points using dynamometer measurements and standard exhaust analyzers. At 5.024 kW, the minimum BSFC was 0.226 $kg \cdot kW^{-1} \cdot h^{-1}$ for TiO_2-conditioned Mahuva, compared with 0.259 $kg \cdot kW^{-1} \cdot h^{-1}$ for diesel, representing a 12.7% reduction and indicating lower fuel consumption per unit brake output. At 5.024 kW, BTE ranged from 28.3 to 31.85% for oxide-conditioned biodiesels and was 34.1% for diesel. Smoke opacity for Al_2O_3-conditioned *Calophyllum* was 8, compared with 9 for diesel. NO levels for most treated blends ranged from 790 to 890 ppm, while one Al_2O_3 + Calophyllum trace reached approximately 980 ppm, indicating overall soot suppression alongside load- and treatment-dependent NO formation. These fixed-dose benchmarks support reproducible screening of biodiesel formulations and provide consistent inputs for combustion–emission model calibration. Future work will focus on dispersion stability during extended operation, injector deposit formation, and particle-number characterization under transient duty cycles.

Keywords: Non-edible biodiesel; Metal-oxide nanoadditives; Compression-ignition engine testing; Load-resolved emissions mapping; Renewable fuel.

1. INTRODUCTION

Compression-ignition engines sustain modern mobility, agriculture, and distributed power with high efficiency and durability. Their widespread use also intensifies the need to control regulated exhaust pollutants. Nitrogen oxides and soot remain difficult to control in diffusion-dominated combustion. Fuel-focused strategies are attractive, avoiding costly and complex hardware changes. Liquid biofuels are particularly relevant because they fit the existing logistics. Biodiesel is a widely studied alternative fuel in this group. It is produced from triglyceride feedstock through transesterification. It contains oxygen within the fuel molecule (Vellaiyan, 2025a). This oxygen supports oxidation reactions during combustion. Biodiesel also provides lubricity, which benefits fuel system components. However, its properties differ from those of petroleum diesel. Viscosity, density, volatility, and heating values commonly shift. These shifts influence the spray breakup, evaporation, and mixture formation. They also influence the ignition delay and heat-release phasing. These coupled effects motivate the formulation-control approach rather than reliance on single-fuel substitution (Arumugam *et al.* 2024).

Non-edible oils have received sustained attention, as they do not directly compete with the food supply. *Calophyllum inophyllum, Nerium oleander,* and *Madhuca indica* (Mahuva) have been reported as viable feedstocks for biodiesel production via transesterification (Aurtherson *et al.* 2024). Prior engine investigations have described the stable operation of these methyl esters under controlled settings. Performance and emission responses have also been reported to be sensitive to the

load and operating conditions. Property-driven mixing limitations have been frequently discussed for low and mid-load. Cold flow behavior and viscosity effects were also observed for specific feedstocks. Additive packages were introduced to address fuel system cleanliness, oxidation stability, and dispersion needs (Nachippan *et al.* 2024). Earlier studies have also applied blending with diesel or oxygenates. The injection timing and pressure adjustments have also been explored in several studies. These efforts have established the feasibility of using non-edible biodiesels. They also indicated that the formulation and operating conditions jointly governed these outcomes. A consistent and comparable framework across multiple feedstocks has not always been established (Janaki *et al.* 2024).

Metal-oxide nanoparticles have been investigated as fuel conditioners because of their surface activity and oxygen-related redox behavior. Al_2O_3, CeO_2, and TiO_2 are the most frequently adopted oxides in engine-focused studies. CeO_2 is linked to oxygen storage and release through Ce^{3+}/Ce^{4+} redox cycling. TiO_2 has been discussed in relation to surface-mediated oxidation and thermal effects. Al_2O_3 was examined as a catalytic support and a heat-transfer modifier. Prior experiments have reported changes in the combustion phasing and regulated emissions. These studies also used different nanoparticle concentrations and dispersion methods. The sonication time, surfactant chemistry, and storage duration varied widely. Some studies have reported limited information on sedimentation control. Many investigations have used a narrow set of load points or feedstocks. Some studies have changed the engine speed, injection settings, or sampling basis between trials. As a result, the clear separation of feedstock effects from conditioning effects remains difficult (Hariram *et al.* 2025).

Several methodological shortcomings persist across the literature. Comparable dosing has not been adopted consistently for oxides and fuels. Dispersion quality has not always been verified through morphology or size statistics. Agglomeration and settling can alter the effective surface area of the fuel phase (Yang *et al.* 2025). This change can alter the catalytic accessibility and transport through fuel lines. Sampling practices also influence measured outcomes. Analyzer warm-up, drift checks, and basis corrections are not always described in sufficient detail. Uncertainty budgets have also been inconsistently presented. These issues limit the reproducibility and cross-study comparisons. They also limited the development of datasets suitable for calibrating combustion models. Thus, the field required a harmonized dataset collected under a single operating map. The need was also extended to multiple non-edible biodiesels tested under identical conditioning protocols. Direct comparison of oxide-conditioned non-edible biodiesels remains limited by inconsistent dosing, dispersion practices, operating points, and measurement protocols (Kumar *et al.* 2025).

This study addresses this gap by applying a fixed-dose conditioning matrix to three non-edible biodiesels and one diesel reference. *Calophyllum*, *Nerium*, and Mahuva methyl esters were selected because their fatty acid profiles differ. These differences produce distinct viscosity–volatility–ignition tendencies. The oxide set was restricted to Al_2O_3, CeO_2, and TiO_2 to represent the contrasting surface chemistry and redox behavior. A single additive dose was retained to stabilize the formulations and maintain comparable handling. A single nanoparticle dose was retained to isolate the oxide and feedstock identities as the dominant factors. A repeatable dispersion protocol was applied for each blend. The experimental program was organized according to a defined brake power schedule. A constant engine speed and single test configuration were maintained. The performance metrics and regulated emission indicators were acquired within the same instrumentation system. Data reduction was also held constant across the fuels. These design choices define the novelty of this study. A unified framework was created for multi-feedstock, multi-oxide comparison under controlled dosing and measurement practices.

The objective of this study was to quantify the steady-state performance and regulated emissions of additive-treated and Al_2O_3-, CeO_2-, and TiO_2-conditioned *Calophyllum*, *Nerium*, and Mahuva biodiesels, relative to diesel, across a prescribed brake-power range.

2. MATERIALS AND METHODS

Petroleum diesel fuel, in compliance with ASTM D975, was used as the reference, and three non-edible biodiesel fuels were prepared from the crude oils of *Calophyllum inophyllum, Nerium oleander,* and *Madhuca indica* (Mahuva). Al_2O_3, CeO_2, and TiO_2 nanopowders were used as oxide modifiers, and a commercial fuel-conditioning additive package was used as a dispersant–detergent–stability additive at a fixed dose. Anhydrous methanol (≥99.8%, Merck, Darmstadt, Germany), sodium hydroxide pellets (≥98%, Merck), and deionized water (18.2 MΩ·cm) were used for transesterification and washing. Nanopowders were procured as commercial grades with certificate-reported purity ≥99% and nominal primary particle size of 20–50 nm. All masses were measured using an analytical microbalance (Mettler Toledo XPR205DR, Mettler Toledo, Columbus, OH, USA; readability 0.01 mg), and all liquid volumes were prepared using Class A volumetric glassware. The material set and nominal specifications used for fuel preparation and conditioning are listed in Table 1. Batch identifiers were assigned to each biodiesel and conditioned blend to preserve traceability through preparation, testing, and data reduction.

Table 1. Raw materials and nominal specifications used for biodiesel synthesis and fuel conditioning

Item	Specifications	Supplier / Standard
Diesel fuel	Ultra-low sulfur diesel	ASTM D975
Calophyllum oil	Non-edible crude oil, filtered	Local supplier
Nerium oil	Non-edible crude oil, filtered	Local supplier
Mahuva oil	Non-edible crude oil, filtered	Local supplier
Methanol	≥99.8% anhydrous	Merck, Germany
Sodium hydroxide	≥98% pellets	Merck, Germany
Al_2O_3 nanopowder	≥99% purity, 20–50 nm	Commercial nanopowder grade
CeO_2 nanopowder	≥99% purity, 20–50 nm	Commercial nanopowder grade
TiO_2 nanopowder	≥99% purity, 20–50 nm	Commercial nanopowder grade
Fuel-conditioning additive	Proprietary package	Commercial additive grade
Deionized water	18.2 MΩ·cm	In-house system

Biodiesel fuels were produced as fatty acid methyl esters via base-catalyzed transesterification. Each crude oil was filtered through a 5 µm membrane and dehydrated under vacuum at 60 °C for 2 h. A methanolic catalyst solution was prepared by stirring sodium hydroxide into anhydrous methanol until complete dissolution. The dehydrated oil was charged into a jacketed glass reactor fitted with a reflux condenser and mechanical agitator, and the temperature was maintained at 60 ± 1 °C using a circulating bath. Methanol was added to achieve a 6:1 methanol-to-oil molar ratio, and the catalyst loading was fixed at 1.0 wt.% relative to the oil mass. The reaction mixture was stirred at 700 rpm for 90 min, transferred to a separation vessel, and left undisturbed for 12 h. The glycerol phase was drained, and the ester phase was washed repeatedly with warm deionized water until the wash water approached neutral pH. Residual water was removed by heating at 105 °C until a constant mass was recorded. The esters were cooled to ambient temperature and stored in amber bottles under nitrogen headspace. The fuel properties required for energy-based calculations were measured prior to engine testing using standardized methods, including the density at 15 °C, kinematic viscosity at 40 °C, and gross heat of combustion. A lower heating value was obtained from the measured gross heat of combustion using the standard water formation correction implemented in the calorimetry software and recorded as the lower heating value (*LHV*), an input for the brake thermal efficiency calculation.

Fuel conditioning was performed by preparing, for each biodiesel, one additive-treated baseline (additive-only) and three oxide-treated blends (Al_2O_3, CeO_2, TiO_2) containing both additive and nanopowder. The additive dose was fixed at 200 mg·L^{-1}, and the nanopowder dose was fixed at 200 mg·L^{-1} for all oxide-treated blends. The concentrations were set gravimetrically from the dosed mass and the prepared fuel volume, using Eq. (1).

$$C = \frac{m}{V} \quad \ldots (1)$$

In Eq. (1), C denotes the mass concentration (mg·L^{-1}), m denotes the dosed mass of additive or nanopowder (mg), and V denotes the prepared fuel volume (L). Fig. 1 illustrates the conditioning workflow for dosing, dispersion, and transfer to the engine day tank, showing the order of weighing, predispersion, ultrasonication, bulk homogenization, and sealed storage before testing. The nanopowders were pre-dispersed into 50 mL aliquots of the target biodiesel under magnetic stirring at 800 rpm for 20 min, and probe ultrasonication was applied at 20 kHz for 15 min using a pulsed duty cycle. The pre-dispersion was transferred into the bulk fuel volume and homogenized using a mechanical overhead stirrer at 600 rpm for 30 min. Then, the additive was dosed, and mixing was maintained for 15 min. The prepared blends were stored in sealed metal containers at laboratory temperature and transferred to the day tank immediately before testing.

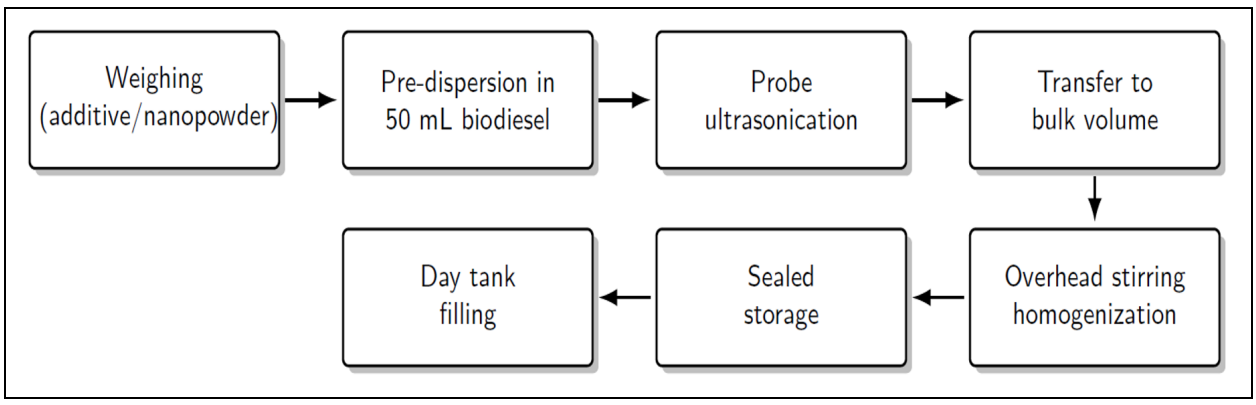


Fig. 1: Fuel additive and nanopowder dispersion workflow

Engine experiments were conducted using a single-cylinder, four-stroke, water-cooled, direct-injection compression-ignition engine coupled to an eddy-current dynamometer. A dynamometer controller regulated speed and load, and a strain-gauge torque transducer was used to measure torque. Airflow was measured using a laminar flow element with a differential pressure transducer, and fuel mass flow was measured using a Coriolis meter. The exhaust gas temperature was measured using a K-type thermocouple inserted into the exhaust duct and conditioned with a thermocouple amplifier. Gaseous emissions were measured using an exhaust gas analyzer suite comprising a non-dispersive infrared (NDIR) analyzer for CO and CO_2, electrochemical sensors for O_2, a flame ionization detector (FID) for total hydrocarbons, and a chemiluminescence analyzer for NO. Smoke was measured using a filter-type smoke meter. The principal instrumentation and nominal metrological specifications are summarized in Table 2 and were used as references for calibration scheduling and uncertainty assignment.

The dynamometer controller maintained a constant engine speed throughout testing, and speed verification was performed using an optical tachometer (Extech 461920) at three set points. The controller scaling was adjusted when deviations exceeded the laboratory acceptance criterion. Testing was performed under steady-state conditions at five brake-power setpoints (BP = 0, 1.256, 2.512, 3.768, and 5.024 kW). After each load change, a 5-min stabilization period was applied. For each setpoint, data were acquired for 180 s at 1 Hz synchronized logging, and reported values were computed as the mean of the final 60 s window. Three independent repeats were performed for each fuel condition. The ambient laboratory temperature was maintained at 25 ± 2 °C. The coolant temperature was regulated using a thermostatic bath connected to the engine jacket, and the fuel temperature at the injection pump inlet was monitored and maintained within ±2 °C. Between fuels, the fuel circuit was flushed with the incoming blend for 10 min, and the engine was operated at low load to reduce carryover within the pump and injector. The operating conditions, stabilization intervals, and acquisition windows are listed in Table 3.

Calibration and verification were performed before each test day and after completion of each fuel family. Fig. 2 shows the experimental engine used in this study. Torque calibration was conducted using a dead-weight arm and a multi-point loading schedule, and the calibration relationship between the torque and sensor output was obtained using linear regression, using Eq. (2).

$$T = aV + b \quad ..(2)$$

In Eq. (2), T denotes brake torque (N·m), V denotes the torque-cell output (V), a denoted the slope (N·m·V^{-1}), and b denotes the intercept (N·m). Speed verification was conducted using an optical tachometer (Extech 461920, Extech Instruments, Nashua, NH, USA) at three set points, and controller scaling was adjusted when deviations exceeded the laboratory acceptance criterion. The fuel mass flow verification was conducted by timed mass collection using an analytical balance and by comparing the measured mass to the Coriolis output over the same interval. The airflow verification was conducted using a secondary flow reference connected to a laminar flow element. Thermocouple verification was conducted using a dry-block calibrator (Fluke 9142, Fluke Corporation, Everett, WA, USA) at 200 °C, 400 °C, and 800 °C, and offsets were applied within the data acquisition (DAQ) scaling configuration. Gas analyzers were warmed for at least 45 min, zeroed using high-purity nitrogen (99.999%), and spanned using certified calibration gases traceable to national standards; heated sampling lines were maintained at 190 °C for the hydrocarbon channel to limit condensation losses, and particulate filters were installed upstream of the analyzers (Sateesh *et al.* 2024).

Table 2. Engine test bench instrumentation, model identifiers, and nominal measurement specifications

Measurement	Instrument (Model)	Maker	Range (Capability / used)	Resolution
Speed	Dynamometer encoder (AG-10)	FH	0–6000 rpm (used: 1500 rpm)	1 rpm
Torque	Torque cell (AG-10)	FH	0–100 N·m	0.01 N·m
Fuel mass flow	Coriolis meter (CMF010M)	MM	used: 0–30 kg·h^{-1}	0.001 kg·h^{-1}
Air mass flow	LFE + differential pressure (M200)	MER	LFE-dependent; ΔP sensor range model-dependent	0.1 Pa
Exhaust temperature	K-type thermocouple + NI-9213	TC/NI	NI-9213: ±78.125 mV input; K-type per NIST range	24-bit ADC
Smoke	Smoke meter (437C)	AVL	Report unit (opacity/BSN/FSN) and span used	Report from the instrument manual

The test bench layout and sensor placement were configured to support the synchronized acquisition of the mechanical, thermal, and emission channels. Fig. 3 shows the bench schematic used for fuel delivery, airflow measurement, exhaust sampling, and signal routing, which identifies the day tank, fuel meter, airflow element, thermocouple position, and analyzer sampling ports. Exhaust sampling was performed using a stainless steel probe inserted into the exhaust duct downstream of the manifold, with the probe outlet connected to the gas analyzers via heated, insulated lines. Smoke sampling was conducted through the smoke meter sampling interface using the instrument's prescribed draw sequence. A common timing signal from the DAQ

chassis was used to time-stamp all channels, and synchronization was verified by applying step changes in the load and observing coincident changes in torque and fuel flow within the same sample index (Bikkavolu *et al.* 2025).



Fig. 2: Experimental engine test rig

The brake power was calculated from the speed and torque, using Eq. (3).

$$BP = \frac{2\pi NT}{60{,}000} \quad \ldots (3)$$

Table 3. Engine operating conditions, boundary settings, and data acquisition schedule used for all fuels

Parameter	Setting
Speed control	Constant speed under dynamometer control
Brake-power setpoints	0, 1.256, 2.512, 3.768, 5.024 kW
Stabilization time per setpoint	5 min
Acquisition duration per setpoint	180 s
Averaging window	final 60 s of each acquisition
Sampling rate	1 Hz synchronized logging
Replication	three independent repeats per fuel condition

In Eq. (3), BP denotes brake power (kW), N denotes engine speed (rev·min^{-1}), and T denotes brake torque (N·m). In the present study, the engine speed N in Eq. (3) was taken as the measured mean speed over the final 60 s averaging window at each brake-power setpoint. Brake-specific fuel consumption was calculated using Eq. (4).

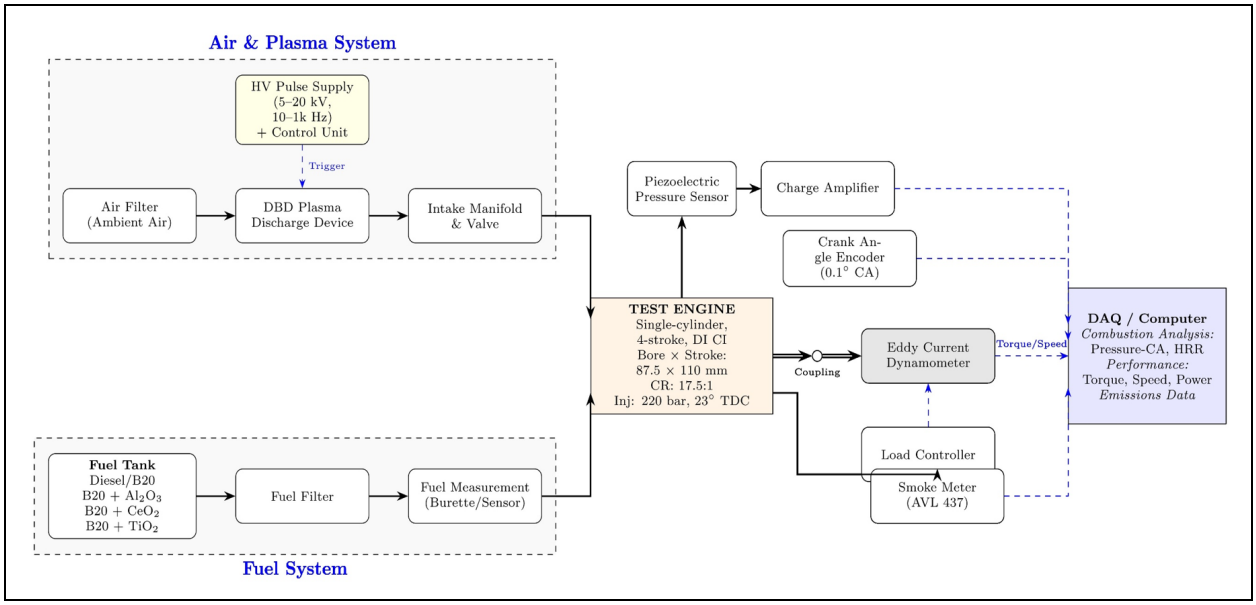


Fig. 3: Engine–dynamometer layout and measurement lines

$$BSFC = \frac{\dot{m}_f}{BP} \quad \ldots (4)$$

In Eq. (4), $BSFC$ denoted brake specific fuel consumption (kg·kW^{-1}·h^{-1}) and $\dot{m}_f$ denotes fuel mass flow rate (kg·h^{-1}). Brake thermal efficiency was calculated using the lower heating value of each tested fuel (Eq. 5).

$$BTE = \frac{BP}{\dot{m}_f \, LHV} \times 100 \quad \ldots (5)$$

BTE denoted brake thermal efficiency (%) and LHV denoted the lower heating value (kJ·kg^{-1}) with consistent unit conversion applied in the computational implementation. Time-window averaging was applied to each raw channel prior to the calculation of the derived metric using Eq. (6).

$$\dot{x} = \frac{1}{n}\sum_{i=1}^{n} x_i \qquad \ldots (6)$$

$\dot{x}$ denotes the window-averaged value of a measured channel, x_i denotes the i-th sample in the window, and n denotes the number of samples in the averaging window. To reduce crowded equation cross-referencing and strengthen traceability between measurements, reduction equations, and uncertainty inputs, the calculation map summarized in Table 4 was used to link each reported quantity to its measured inputs, acquisition step, and uncertainty source, which was cited at the point where the associated metric was first described.

Table 4. Calculation map linking measured channels, data-reduction equations, and uncertainty propagation inputs for reported metrics

Reported Quantity	Reduction Equation	Primary Measured Inputs	Reduction Step	Calibration Linkage Source
Brake power	(3)	N (rpm), T (N·m)	Window average → compute BP	Torque dead-weight; tachometer check
BSFC	(4)	$\dot{m}_f$ (kg·h⁻¹), BP (kW)	Window average → compute $BSFC$	Gravimetric fuel-flow verification
BTE	(5)	BP (kW), $\dot{m}_f$ (kg·h⁻¹), LHV (kJ·kg⁻¹)	Compute BTE with unit conversion	Calorimetry method and repeats
Exhaust temperature	—	T_{exh} (°C)	Window average	Dry-block verification
CO, HC, NO	—	Analyzer outputs	Zero/span corrected → window average	Certified gases; drift check
Smoke	—	Smoke index	Instrument protocol → recorded value	Optical reference routine

Uncertainty analysis was executed as a distinct workflow applied after data reduction, and was tied to the same measured input set summarized in Table 4. The combined standard uncertainty of the derived quantity $y = f(x_1, \ldots, x_p)$ was calculated using first-order propagation, as expressed in Eq. (7).

$$u_c(y) = \sqrt{\sum_{j=1}^{p}\left(\frac{\partial f}{\partial x_j}\right)^2 u^2(x_j)} \qquad \ldots (7)$$

In Eq. (7), $u_c(y)$ denotes the combined standard uncertainty in units of y, $x_j$denotes the j-th input variable, $u(x_j)$ denotes the standard uncertainty of x_j, and p denotes the number of inputs. The expanded uncertainty was calculated using Eq. (8), with a coverage factor, $k = 2$.

$$U = k\, u_c(y) \qquad \ldots (8)$$

In Eq. (8), U denotes the expanded uncertainty and k denotes the coverage factor (dimensionless). The uncertainty in brake power was calculated by applying Eq. (7) to Eq. (3), yielding Eq. (9).

$$u_c(BP) = \sqrt{\left(\frac{2\pi T}{60\,000}\, u(N)\right)^2 + \left(\frac{2\pi N}{60\,000}\, u(T)\right)^2} \qquad \ldots (9)$$

In Eq. (9), $u(N)$ denotes the standard uncertainty of speed (rev·min⁻¹) and $u(T)$ denotes the standard uncertainty of torque (N·m). The uncertainty in the BSFC was calculated by applying Eq. (7) to Eq. (4), yielding Eq. (10):

$$u_c(BSFC) = \sqrt{\left(\frac{1}{BP}\, u(\dot{m}_f)\right)^2 + \left(\frac{\dot{m}_f}{BP^2}\, u(BP)\right)^2} \qquad \ldots (10)$$

In Eq. (10), $u(\dot{m}_f)$ denotes the standard uncertainty of fuel mass flow rate (kg·h⁻¹). The uncertainty in the BTE was calculated by applying Eq. (7) to Eq. (5), yielding Eq. (11):

$$u_c(BTE) = \sqrt{\left(\frac{100}{\dot{m}_f\, LHV}\, u(BP)\right)^2 + \left(\frac{100\, BP}{\dot{m}_f^2\, LHV}\, u(\dot{m}_f)\right)^2 + \left(\frac{100\, BP}{\dot{m}_f\, LHV^2}\, u(LHV)\right)^2} \qquad \ldots (11)$$

In Eq. (11), $u(LHV)$ denotes the standard uncertainty of the lower heating value (kJ·kg⁻¹) obtained from the repeated calorimetry and instrument specifications (Demirtaş *et al.* 2024). Replication was implemented in three independent repeats per fuel condition, as defined in Table 3, and repeatability was quantified using the sample standard deviation expressed in Eq. (12).

$$s = \sqrt{\frac{\sum_{i=1}^{n}(x_i - \dot{x})^2}{n-1}} \qquad \ldots (12)$$

In Eq. (12), s denotes the sample standard deviation, x_i denotes the i-th replicate value, $\dot{x}$ denotes the replicate mean, and n denotes the number of replicates.

Nanopowder morphology and agglomerate statistics were documented using scanning electron microscopy and image-based measurements, with the procedure confined to acquisition and quantification. SEM imaging was performed using a field-emission SEM (FEI Quanta 250 FEG, Thermo Fisher Scientific, Hillsboro, OR, USA) operated at 5–10 kV for morphological imaging and 15 kV for EDX confirmation, with a working distance of 8–10 mm. The samples were prepared by depositing a small quantity of nanopowder onto conductive carbon tape on aluminum stubs, and Au/Pd sputter coating was applied using a Quorum Q150R ES (Quorum Technologies, Laughton, UK) with a nominal thickness of 5 nm to reduce charging. Fig. 4 presents a schematic of the SEM image-processing pipeline used for scale calibration, segmentation, equivalent circular diameter (ECD) computation, and percentile extraction, which identifies the sequence used to convert grayscale micrographs into binary masks and measured objects without introducing mechanistic interpretation. Image analysis was conducted using ImageJ (National Institutes of Health, Bethesda, MD, USA) for thresholding and particle labeling, and batch calculations were performed using Python for distribution and percentile extraction.

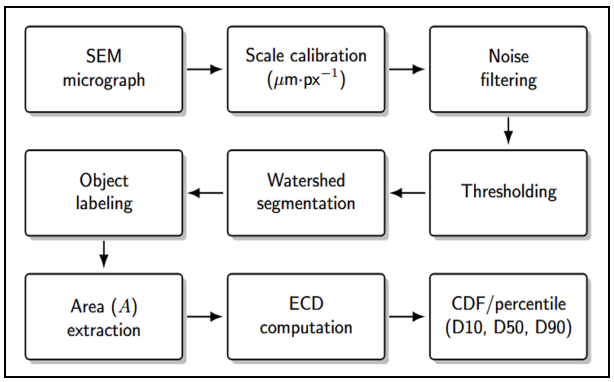


Fig. 4: SEM segmentation and ECD extraction workflow

The equivalent circular diameter is computed from the segmented object area, as expressed in Eq. (13).

$$ECD = \sqrt{\frac{4A}{\pi}} \quad \ldots (13)$$

In Eq. (13), ECD denotes the equivalent circular diameter (μm), and A denotes the segmented projected area (μm²) obtained after pixel-to-length conversion using the calibrated scale. Percentiles were extracted from the empirical cumulative distribution function, $F(d)$, of the measured ECD values by identifying diameters, D_p, satisfying $F(D_p) = p/100$, and the extraction algorithm was implemented consistently across the oxides using the same thresholding strategy and watershed settings recorded in the analysis log.

3. RESULTS AND DISCUSSION

Fig. 5 illustrates the SEM-derived agglomerate morphology, along with ECD statistics from segmented boundaries, presented as a cumulative distribution function (CDF) and frequency histograms for the three oxide nanopowders. Fig. 5 (a) displays densely clustered Al_2O_3 agglomerates with segmentation outlines that partition contiguous clusters into discrete objects, and the measured dataset indicated n = 379 with a mean ECD of 2.07 μm, D10 = 0.87 μm, D50 = 1.82 μm, and D90 = 3.73 μm, while the histogram retains a right-skewed tail extending toward ~7 μm. Fig. 5 (b) shows CeO_2 agglomerates with a similar clustered topology but with a slightly shifted distribution toward a smaller median size, and the measurements indicated n = 424 with a mean ECD of 2.09 μm, D10 = 0.85 μm, D50 = 1.75 μm, and D90 = 3.81 μm; the cumulative curve rises rapidly below ~3 μm and then approaches saturation gradually, consistent with a minority population of larger agglomerates. Fig. 5 (c) presents TiO_2 agglomerates with segmentation that yields larger enclosed regions at a comparable imaging scale, and the measurements indicated n = 367 with a mean ECD of 2.31 μm, D10 = 0.87 μm, D50 = 2.06 μm, and D90 = 4.12 μm, accompanied by a broader upper tail and sustained counts above ~3 μm. These trends suggest that TiO_2 formed the largest characteristic agglomerates, which implies a reduced external surface-to-volume ratio and an elevated propensity for gravitational settling during liquid-phase dispersion. The lower D50 values for CeO_2 and Al_2O_3 imply a larger fraction of smaller agglomerates that can sustain suspension stability under identical mixing and ultrasonication protocols. The shared right-skewed distributions across Figs. 5 a–c indicate that agglomeration governs the effective particle size relevant to fuel handling and catalytic accessibility, and the distinct D90 ranking (TiO_2 > CeO_2 > Al_2O_3) highlights oxide-dependent cohesion, which is expected to influence repeatable dosing, injector-line transport, and the persistence of active surface area during engine operation.

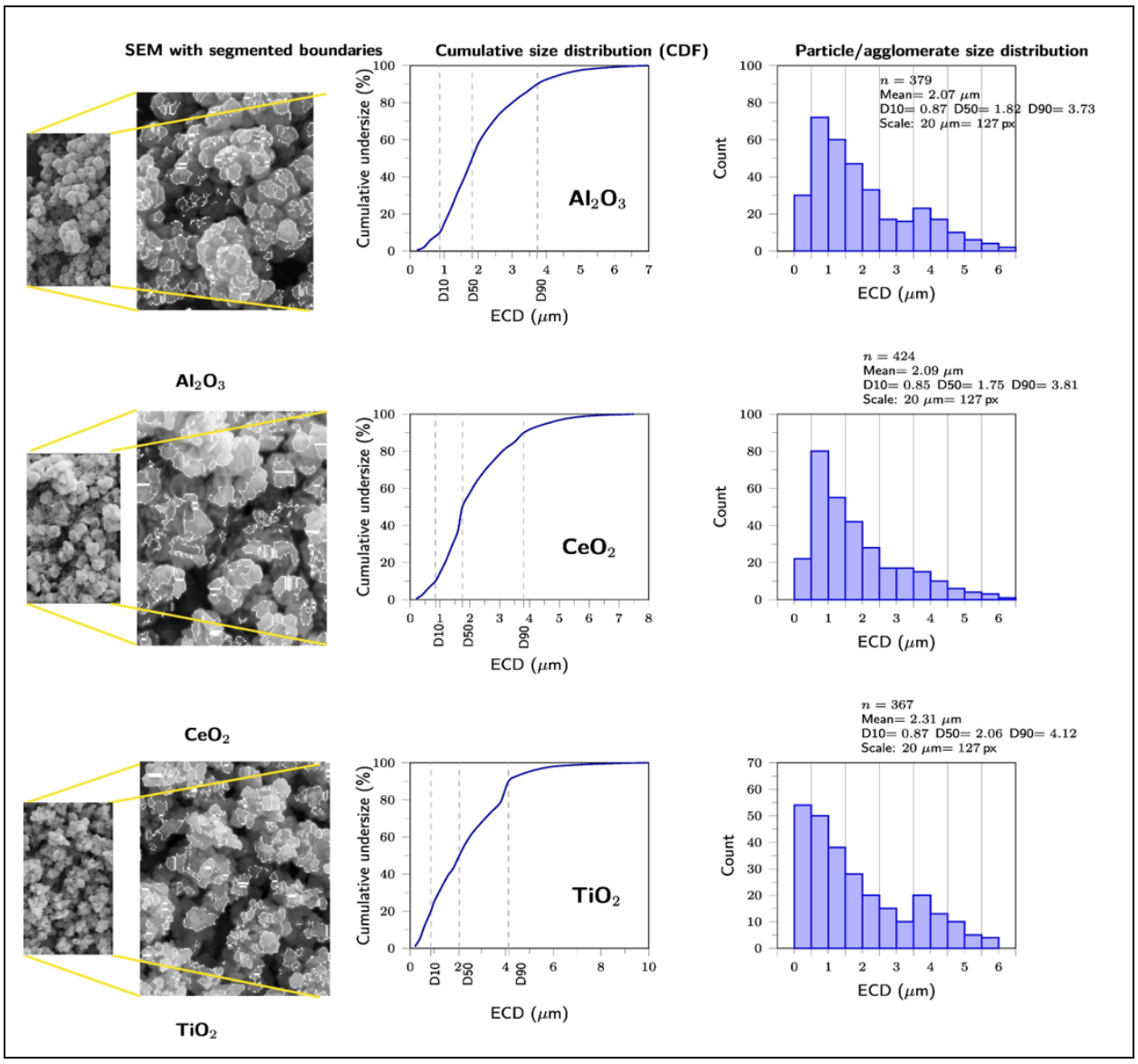


Fig. 5: (a) Al_2O_3 ECD CDF and histogram, (b) CeO_2 ECD CDF and histogram and (c) TiO_2 ECD CDF and histogram

Diesel-referenced quantitative comparisons were used to support each stated trend in the matched brake power. The percentage change relative to diesel was defined as, $\Delta(\%) = \frac{X_i - X_{diesel}}{X_{diesel}} \times 100$, where X_i was the measured response for a given formulation and X_{diesel} was the diesel value at the same operating point. The absolute values and corresponding $\Delta(\%)$ values were reported for each response at BP = 5.024 kW to provide a single-load anchor for cross-fuel comparison. Textual comparisons were aligned with these normalized values such that each increase or decrease was traceable to a specified magnitude.

Fig. 6 illustrates the comparative BP-dependent BSFC behavior of diesel and the three non-edible biodiesels with nanoparticle-conditioned formulations. The BSFC rises sharply from the zero-load point to a local maximum at BP = 1.256 kW and then declines with further loading toward BP = 5.024 kW. The experiments yielded peak BSFC values clustered near 0.62–0.66 kg·kW^{-1}·h^{-1} at BP = 1.256 kW, followed by a reduction to 0.33–0.40 kg·kW^{-1}·h^{-1} at BP = 2.512 kW. At BP = 3.768 kW, most curves remain within about 0.28–0.34 kg·kW^{-1}·h^{-1}, while one TiO_2-conditioned *Nerium* trace retained a higher mid-load level near 0.36 kg·kW^{-1}·h^{-1}. At BP = 5.024 kW, the dataset converged toward 0.23–0.27 kg·kW^{-1}·h^{-1}, indicating a narrowing of fuel-to-fuel separation as load increased. This load response is consistent with the physics of compression-ignition operation, in which indicated work rises faster than parasitic losses as torque increases, and the ratio, $BSFC = \dot{m}_f / BP$, decreases, as expressed by Eq. (4) used in the reduction workflow. The low-load peak suggests that mixing-controlled combustion and wall heat losses limit the effective conversion when the injected mass per cycle is small, whereas a higher load promotes a higher

in-cylinder temperature and faster oxidation kinetics, reducing the fuel mass required per unit brake output. The modest dispersion of the nanoparticle-conditioned curves around the base biodiesel traces suggests that catalytic oxygen buffering, altered spray microstructure, and rheology-driven changes in atomization acted together, with CeO_2 and Al_2O_3 trends aligning with slightly reduced BSFC at higher loads for selected fuels, whereas TiO_2 conditioning introduced a fuel-specific mid-load deviation that is consistent with sensitivity to dispersion stability and viscosity-mediated injection dynamics (Jayabal and Rajkumar, 2025).

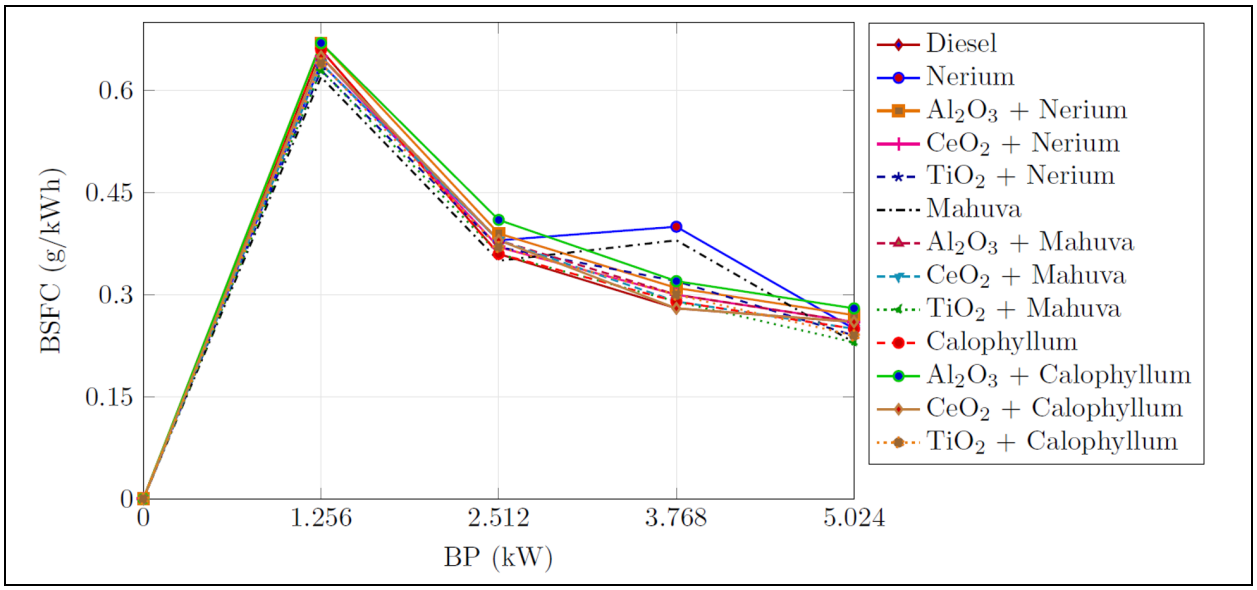


Fig. 6: BSFC vs. brake power

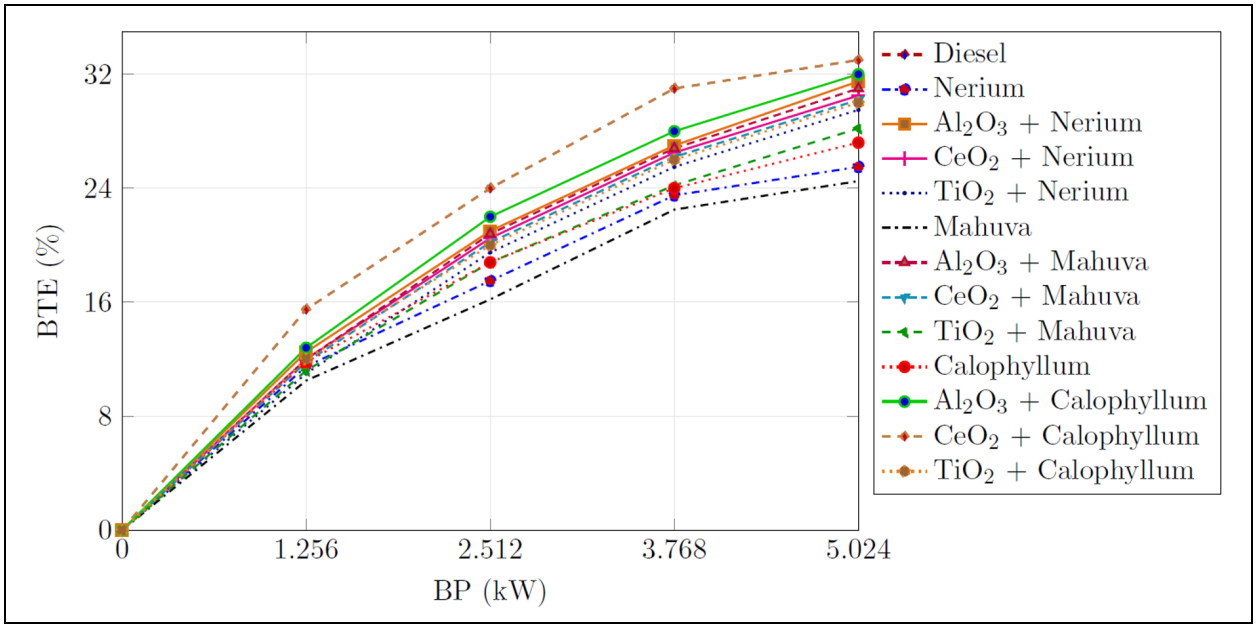


Fig. 7: BTE vs. brake power

Fig. 7 illustrates the BP-dependent evolution of brake thermal efficiency for diesel and the three non-edible biodiesels under baseline additive conditioning and oxide-nanoparticle treatments. The curves increase monotonically with the brake power, with the steepest rise between BP = 0 and 1.256 kW and a progressively reduced slope toward BP = 5.024 kW. The experiments indicated that diesel maintained the highest BTE at each loaded point, reaching 16% at 1.256 kW, 24% at 2.512 kW, 31–32% at 3.768 kW, and 34% at 5.024 kW, whereas biodiesel-based fuels populated a lower band that expanded at mid-load and tightened at the highest load. At BP = 1.256 kW, the biodiesel and treated-biodiesel traces clustered near 10–13%, and at BP = 2.512 kW, they

spread to 16–22%, reflecting fuel-specific sensitivity to combustion phasing and mixing quality, which were strongly load dependent. At BP = 3.768 kW, several nanoparticle-conditioned blends approached the upper portion of the biodiesel band by 27–29%, whereas the lower envelope remained near 23–25%. At BP = 5.024 kW, the upper biodiesel traces reached 31–32%, while the lowest remained near 25–26%, indicating that the separation persisted but decreased relative to the absolute efficiency scale at a high load (Priya and Ranjitha, 2025). This load response aligns with the definition of brake thermal efficiency, $BTE = \frac{BP}{\dot{m}_f LHV} \times 100$, because increasing the brake power reduces the fractional influence of friction and wall heat transfer while sustaining a higher in-cylinder temperature that supports faster oxidation kinetics and reduced late-cycle heat release. The treatment-dependent ordering suggests that oxide nanoparticles modify the effective combustion process through the combined catalytic activity, oxygen-buffering behavior, and altered spray microstructure, thereby shifting the ignition delay and diffusion-flame oxidation rates in a fuel-dependent manner (Raviteja *et al.* 2024).

Measurement uncertainty was used to contextualize the discussion of small separations among the curves. Expanded uncertainty bounds for speed, torque, fuel flow, temperature, and gas analyzers were treated as limits for distinguishing differences, and curve separations comparable to these bounds were described as indistinguishable within the measurement constraints. The uncertainty magnitudes used for interpretation are summarized in Table 5, and statements describing marginal differences were constrained to comparisons that exceeded the stated expanded uncertainty.

Table 5. Expanded uncertainty bounds (k = 2)

Quantity	Uncertainty Basis	Expanded Uncertainty, U (k = 2)
Speed, N	Encoder verification	±0.2% of reading
Torque, T	Dead-weight calibration	±0.5% of reading
Fuel mass flow, $\dot{m}_f$	Meter verification	±0.5% of reading
Exhaust gas temperature, EGT	Thermocouple calibration	±2 °C
CO	NDIR zero/span specifications	±2% of reading
HC	FID zero/span specifications	±2% of reading
NO	Chemiluminescence zero/span specifications	±2% of reading
Smoke	Smoke meter specifications	±2% of reading

Mechanistic discussions were constrained to an evidence-supported interpretation derived from measured outputs. Catalytic surface effects and oxygen-buffering behavior were treated as literature pathways rather than as directly verified causation because in-cylinder pressure traces, heat-release reconstruction, and post-test surface chemistry were not included in the measurement set. Interpretations were framed in terms of consistency between the observed load-dependent responses and established redox and surface-oxygen concepts reported for oxide additives, while the primary emphasis remained on experimentally quantified performance and emission metrics. The persistence of a diesel advantage across the full load range suggests that differences in spray formation, volatility distribution, and combustion completeness remained influential even after additive and nanoparticle conditioning, while the curves at higher loads indicate that thermochemical conditions increasingly dominated the fuel property effects (Kanwal *et al.* 2025).

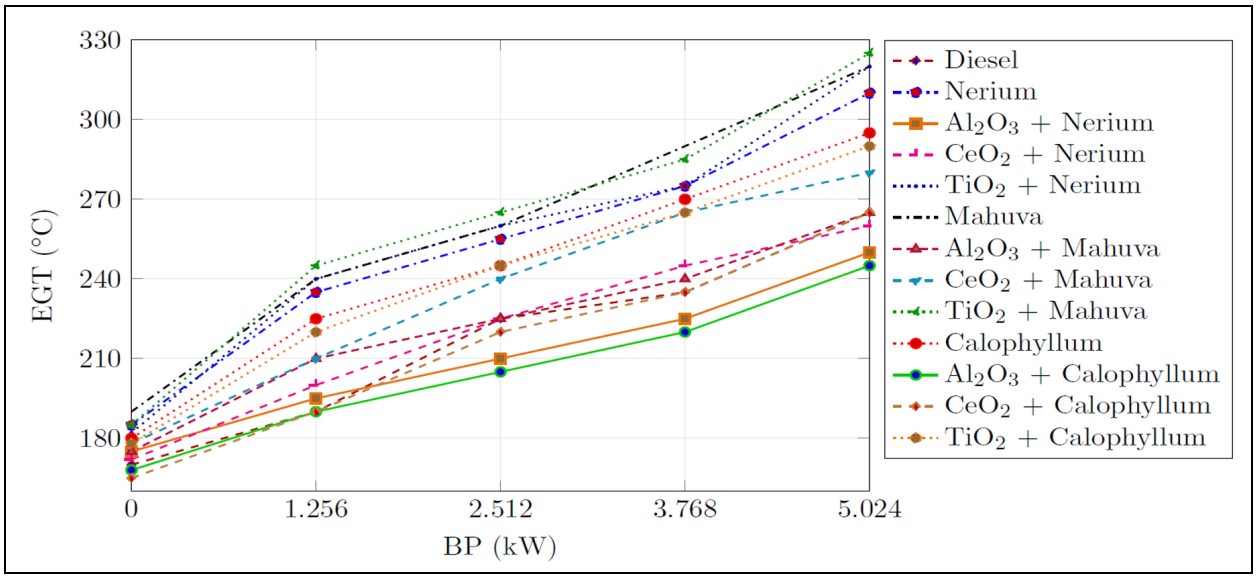


Fig. 8: EGT vs. brake power

Fig. 8 illustrates the load-dependent evolution of exhaust gas temperature for diesel and the three biodiesel fuels under baseline additive conditioning and oxide-nanoparticle treatments. The EGT increases monotonically with brake power across all fuels, and the separation among curves widens as BP increases. The experiments indicated that diesel sustained the lowest exhaust temperatures across the operating range, increasing from 165 to 170 °C at BP = 0 kW to 265–270 °C at BP = 5.024 kW. The biodiesel baselines produced higher EGT than diesel at each loaded point, with *Calophyllum* increasing from ~180 °C at BP = 0 to ~295 °C at BP = 5.024 kW, *Nerium* increasing from ~175 °C to ~310 °C, and Mahuva increasing from ~190 °C to ~320 °C. Within each biodiesel family, Al_2O_3-conditioned traces remained at the lower envelope of the treated set, reaching 245–255 °C at BP = 5.024 kW, while CeO_2-conditioned traces occupied intermediate positions and TiO_2-conditioned traces shifted toward the upper envelope, reaching 290–330 °C at BP = 5.024 kW, depending on the feedstock (Yusuf *et al.* 2022). These patterns suggest that the additive–nanoparticle systems altered the distribution of the released chemical energy between the indicated work, wall heat transfer, and exhaust sensible enthalpy. A higher EGT is consistent with a larger fraction of heat release occurring later in the expansion stroke or with reduced in-cylinder heat extraction, both of which elevate exhaust enthalpy at the valve. The stronger EGT rise for Mahuva and *Nerium* suggests a greater sensitivity of their spray–evaporation–mixing sequence to fuel viscosity and volatility, which can shift combustion phasing and sustain elevated exhaust temperatures at higher loads. The ordering of Al_2O_3 < CeO_2 < TiO_2 within each fuel suggests that varying catalytic and thermal-transport influences governed oxidation intensity and late-cycle burn duration, with TiO_2-associated behavior consistent with sustained high-temperature exhaust flow, and Al_2O_3-associated behavior consistent with reduced exhaust temperature under identical brake-power demand (Patel and Patel, 2025).

Fig. 9 illustrates a monotonic decrease in CO with increasing BP for each fuel, with the largest separation at low loads and progressive convergence at high loads. The experiments indicated that diesel decreased from 0.30% at BP = 0 to 0.12% at BP = 5.024 kW, establishing the lowest baseline across most operating points. The uncoated biodiesel baselines remained higher than diesel at each load, declining from 0.35–0.38% at BP = 0 to about 0.18–0.22% at BP = 5.024 kW, with Mahuva retaining the highest CO envelope and *Calophyllum* forming the lowest biodiesel envelope. Nanoparticle conditioning shifted the biodiesel curves downward at all loads, and the magnitude of the reduction depended on the oxide type and feedstock. Al_2O_3 conditioning produced the strongest suppression, yielding terminal CO levels near 0.10% for Al_2O_3 + *Calophyllum*, about 0.15% for Al_2O_3 + *Nerium*, and about 0.17% for Al_2O_3 + Mahuva at BP = 5.024 kW, while CeO_2- and TiO_2-conditioned fuels clustered at intermediate values near 0.16–0.20% at the same point. The load dependence is consistent with CO oxidation kinetics, which accelerate with an increase in in-cylinder temperature and extended high-temperature residence, thereby reducing the fraction of partially oxidized products discharged at the exhaust valve (Lionus *et al.* 2023). The higher CO levels for the biodiesel baselines suggest that viscosity- and volatility-driven changes in the spray breakup and local equivalence ratio distribution sustained fuel-rich pockets at low and mid load, despite the intrinsic fuel-bound oxygen that supports oxidation in well-mixed regions. The downward shifts produced by oxide conditioning suggest that heterogeneous catalytic pathways and oxygen buffering enhanced the conversion of CO to CO_2 in the diffusion-flame and post-flame zones, while also implying improved microscale mixing through altered droplet behavior and reduced quench-layer persistence. The persistence of Mahuva as the upper envelope across treatments indicated that feedstock-specific physical properties continued to shape local mixing and late-cycle oxidation, even under identical dosing and dispersion protocols (Prakash *et al.* 2024).

Fig. 10 illustrates the strong load dependence of HC, with all curves descending as BP increased and with the steepest reduction occurring between BP = 1.256 and 2.512 kW. The measured outcomes indicated that diesel started near 50 ppm at BP = 0 and declined to 20 ppm at BP = 5.024 kW, whereas the uncoated biodiesel baselines occupied a higher band, decreasing from 65 to 69 ppm at BP = 0 to 28–31 ppm at BP = 5.024 kW. The nanoparticle-conditioned fuels remained within the diesel and uncoated biodiesel envelopes across most loads, and the spread narrowed progressively at high BP, where the lowest-treated cases approached the diesel level. At BP = 0, the Al_2O_3-treated blends yielded the lowest HC within the treated set for each feedstock, with values near 55–61 ppm, while the CeO_2-treated and TiO_2-treated blends occupied higher positions near 59–68 ppm. At BP = 2.512 kW, diesel remained near 31 ppm, Al_2O_3 + *Calophyllum* reached 30 kW, and the remaining treated blends clustered near 32–39 kW, with uncoated Mahuva retaining a higher level near 45 kW. At BP = 5.024 kW, diesel remained near 20 ppm, Al_2O_3 + *Calophyllum* also reached about 20 ppm, Al_2O_3-treated *Nerium* and Mahuva remained near 22–24 ppm, CeO_2-treated cases clustered near 22–24 ppm, and TiO_2-treated cases remained near 25–28 ppm, while uncoated fuels remained near 28–31 ppm. These patterns suggest that the rising load increased the in-cylinder temperature and oxidation residence time, reducing quench-layer survival and limiting the discharge of partially reacted fuel fragments(Manalu *et al.* 2025). The consistently higher HC of uncoated biodiesels indicates that feedstock-

dependent viscosity and volatility affect spray breakup and wall interactions, sustaining localized over-rich or quenched zones at low and moderate loads. The downward shifts produced by oxide additions suggest enhanced post-flame oxidation through catalytic surface pathways and oxygen availability in diffusion-controlled regions, with Al_2O_3-associated behavior aligning with the strongest suppression and TiO_2-associated behavior aligning with a weaker reduction. In contrast, Mahuva retained the upper envelope across treatments, consistent with persistent mixing- and evaporation-related constraints under identical dosing (Jayabal, 2025).

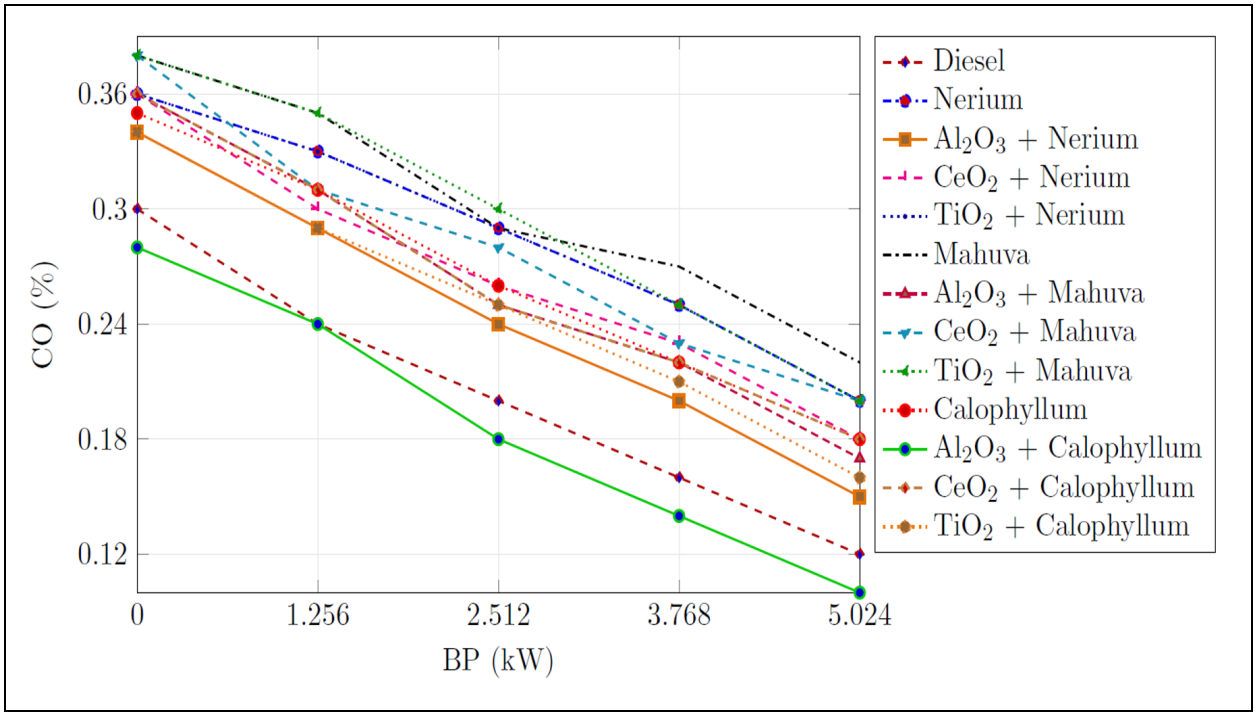


Fig. 9: CO vs. brake power

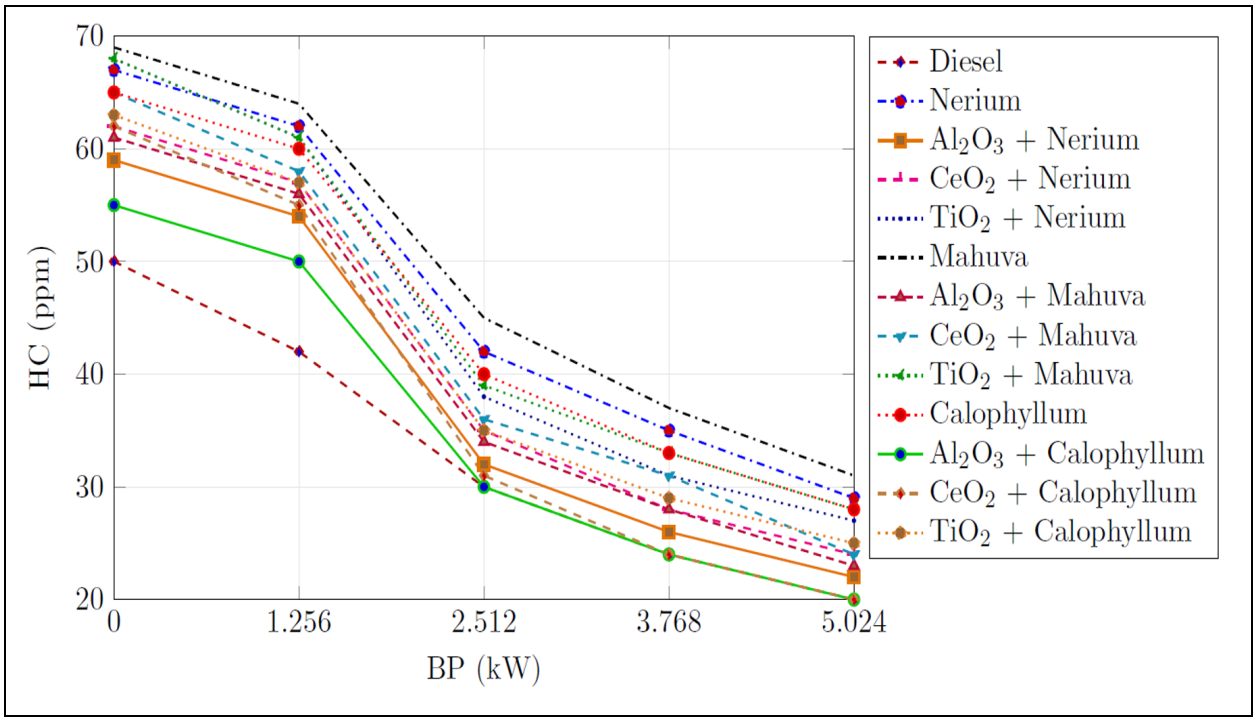


Fig. 10: HC vs. brake power

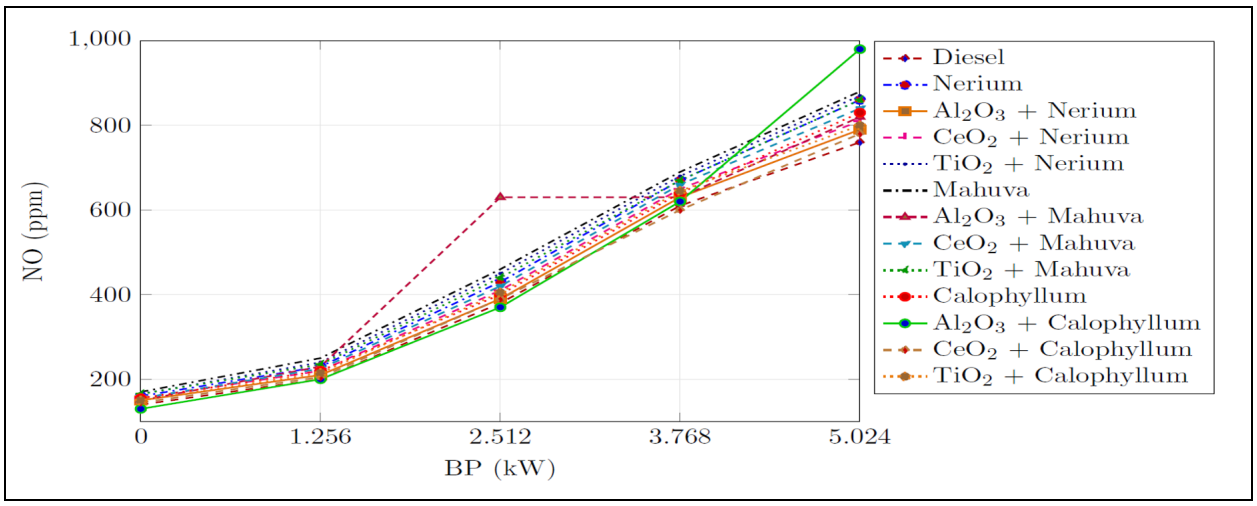


Fig.11: NO vs. brake power

Fig. 11 illustrates a strong monotonic increase in NO with brake power across all fuels, with divergence among formulations becoming pronounced at mid- to high loads. NO levels increased with engine load for both fuels. For diesel, NO rose from 138–150 ppm at BP = 0 kW to 760–790 ppm at BP = 5.024 kW. For uncoated biodiesel, NO increased from 145–165 ppm at BP = 0 kW to 810–880 ppm at BP = 5.024 kW, exceeding diesel at full load. Most nanoparticle-conditioned blends exhibited similar increasing NO trends, clustering tightly up to BP = 1.256 kW with values around 190–246 ppm. Beyond this load, the curves diverged, reaching 370–449 ppm at BP = 2.512 kW and 600–673 ppm at BP = 3.768 kW. At BP = 5.024 kW, most treated blends grouped between 790 and 890 ppm, whereas one Al_2O_3 + *Calophyllum* trace reached the highest measured value of approximately 980 ppm, indicating a distinct high-load deviation relative to the other treatments. A second notable feature is a step-like increase for Al_2O_3 + Mahuva at BP = 2.512 kW, where NO rises to 628 ppm and then remains aligned with the higher-load cluster, suggesting a localized shift in NO formation at this intermediate load.

These trends are consistent with temperature-sensitive thermal NO pathways, in which the formation rates scale strongly with the peak burned gas temperature and oxygen availability, and therefore increase with increased fueling and higher in-cylinder temperature at elevated loads (Gadhave *et al.* 2025). The higher NO levels for biodiesel-based fuels at high BP suggest that fuel-bound oxygen and enhanced oxidation intensity sustained higher local oxygen concentrations in high-temperature zones, thereby increasing the extent of thermal NO formation when the residence time was sufficient. The treatment-dependent spread suggests that oxide nanoparticles modify the heat-release phase and local temperature fields through combined catalytic oxidation and altered spray microstructure, thereby affecting the balance between peak temperature, oxygen availability, and residence time, which governs NO kinetics. The anomalous excursions for Al_2O_3 + *Calophyllum* and Al_2O_3 + Mahuva suggest sensitivity to dispersion stability, local equivalence-ratio stratification, or load-specific combustion phasing shifts that intensify high-temperature regions at the corresponding operating points (Vellaiyan, 2025b).

Fig. 12 illustrates a consistent decrease in smoke with increasing brake power across all fuels, with the steepest drop between BP = 0 and 1.256 kW, followed by a sustained downward trend toward BP = 5.024 kW. The measured results indicated that diesel decreased from 30% at BP = 0 to 9% at BP = 5.024 kW, defining the lowest smoke boundary at a high load. The uncoated biodiesel baselines produced higher smoke than diesel across the load range, declining from 34-38% at BP = 0 to 16–20% at BP = 5.024 kW, with Mahuva retaining the highest smoke envelope and *Nerium* occupying the upper portion of the biodiesel band. Nanoparticle conditioning reduced smoke relative to the corresponding uncoated fuels at all loads, and the reductions became more evident beyond BP = 2.512 kW, as the treated curves separated downward from the baseline biodiesel traces. At BP = 1.256 kW, the treated fuels clustered near 20–27%, while the uncoated fuels remained near 24–32%; at BP = 5.024 kW, the treated set spanned 10–17%, with Al_2O_3 + *Calophyllum* reaching the lowest value near 8%. The oxide-dependent ordering within each feedstock consistently placed the Al_2O_3-conditioned blends toward the lower smoke envelope, CeO_2-conditioned blends in an intermediate band, and TiO_2-conditioned blends toward the upper treated band. These trends suggest that increased load increases in-cylinder temperature and oxidation rates, promoting soot burnout during the expansion stroke and reducing the surviving particulate fraction (as measured by exhaust smoke (Lionus *et al.* 2023). The higher smoke levels for uncoated biodiesel fuels indicate that spray and mixing constraints

associated with viscosity and volatility sustained locally rich diffusion flames and soot precursor formation at low and moderate loads. The reductions produced by oxide conditioning suggest intensified soot oxidation through catalytic surface pathways and oxygen availability in the soot-rich zones, with Al_2O_3-associated behavior aligning with the strongest soot suppression tendency and TiO_2-associated behavior aligning with a weaker suppression. The persistent upper envelope for Mahuva across treatments indicates that feedstock-specific mixture preparation continued to govern soot formation even under identical dosing and dispersion conditions.

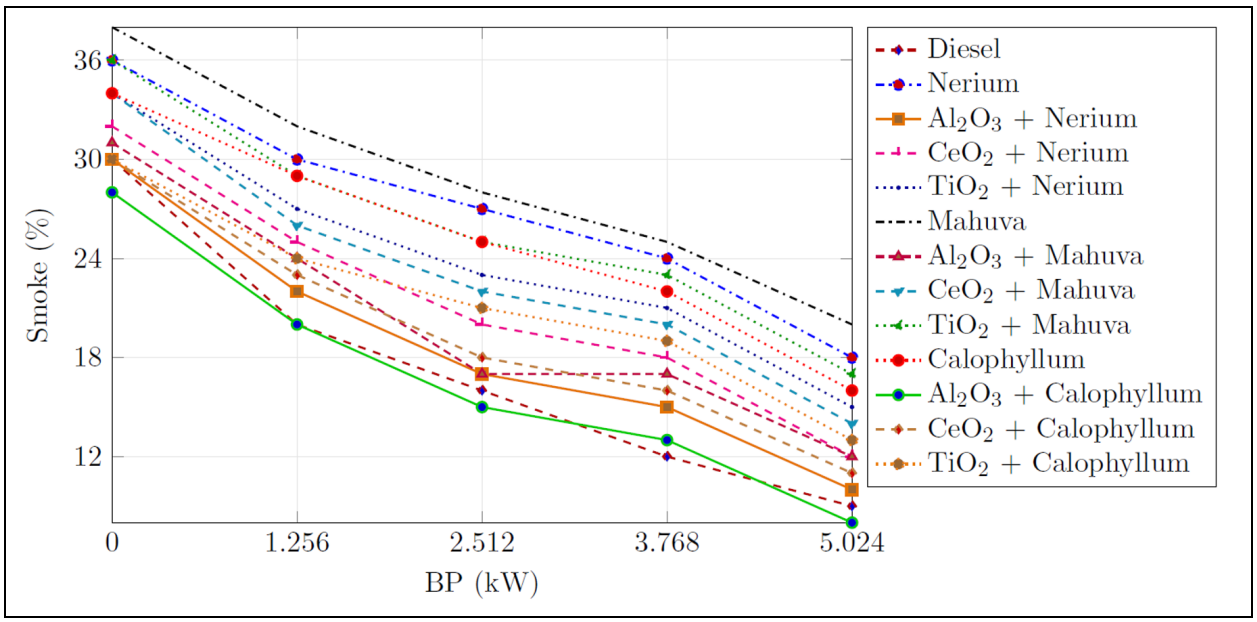


Fig. 12: Smoke vs. brake power

4. CONCLUSION

Additive-treated and oxide-nanoparticle-conditioned biodiesels from *Calophyllum*, *Nerium*, and Mahuva were compared with diesel on a constant-speed, steady-state compression-ignition test bench using fixed additive and oxide-nanoparticle dosing of 200 $mg \cdot L^{-1}$ additive and 200 $mg \cdot L^{-1}$ Al_2O_3, CeO_2, or TiO_2. Across the full brake-power range, a low-load BSFC peak and a progressive decline with increasing load were recorded for all fuels, whereas BTE increased with load for every formulation. At BP = 3.768 kW, diesel delivered a BSFC of 0.273 $kg \cdot kW^{-1} \cdot h^{-1}$ with a BTE of 30.98%, whereas Al_2O_3-conditioned *Calophyllum* delivered a BSFC of 0.325 $kg \cdot kW^{-1} \cdot h^{-1}$ with a BTE of 27.89%, confirming persistent fuel-property influences under identical operating control. The exhaust sensible enthalpy increased with load and remained formulation-dependent, with EGT at BP = 5.024 kW recorded as 265 °C for diesel, 245 °C for Al_2O_3-conditioned *Calophyllum*, and 325 °C for TiO_2-conditioned Mahuva. Incomplete-combustion markers were reduced by oxide conditioning in a feedstock-specific manner: at BP = 5.024 kW, CO was 0.12% for diesel and 0.22% for uncoated Mahuva, while 0.10% was recorded for Al_2O_3-conditioned *Calophyllum*; HC was 20 ppm for diesel and 31 ppm for uncoated Mahuva, while 20 ppm was recorded for Al_2O_3-conditioned *Calophyllum*. The smoke at BP = 2.512 kW was 16% for diesel and 25% for uncoated *Calophyllum*, while 15% was recorded for Al_2O_3-conditioned *Calophyllum*. NO formation increased with load and retained sensitivity to oxide–feedstock pairing, with uncoated biodiesels at BP = 2.512 kW recorded in the 370–449 ppm band and Al_2O_3-conditioned Mahuva at 628 ppm. These outcomes provide a controlled formulation-level basis for selecting oxide conditioning strategies and calibrating predictive combustion–emission models for treated non-edible biodiesels. Future work could focus on quantifying dispersion stability during extended operation, tracking injector deposit evolution, and measuring particle-number-resolved particulate emissions under both steady and transient duty cycles.

FUNDING

This research received no specific grant from any funding agency in the public, commercial, or not-for-profit sectors.

CONFLICTS OF INTEREST

The authors declare that there is no conflict of interest.

COPYRIGHT

This article is an open-access article distributed under the terms and conditions of the Creative Commons

Attribution (CC BY) license (http://creativecommons.org/licenses/by/4.0/).



REFERENCES

Arumugam, H., Pandian, B., Muthaiyan, R., Arumugam, S., Rajendran, S. and Prakash, C., Impact on Green Synthesised Al_2O_3 Nanoparticles on Performance and Emission Properties as Biodiesel operated diesel engine, *Global Nest J.,* 26(10), 06425(2024). https://doi.org/10.30955/gnj.06425

Aurtherson, B. P., Dinesh Babu, D. B., Jayabal, R. and Yuvarajan, Y., Performance and Emission Characteristics of a CRDI Diesel Engine Fuelled by SiO_2 Nanoparticle-Waste Fat Biodiesel Blends, *China Petrol. Proce. Petrochem. Technol.,* 26(1), 56–66(2024).

Bikkavolu, J. R., Tota, R. K., H, R., Chebattina, K. R., Bhagavatula, L. R., Pullagura, G. and Seepana, P. K., Predicting Common Rail Direct Injection (CRDI) engine metrics using nanoparticle-enhanced pongamia pinnata biodiesel with machine learning, *Emergent Mater.,* 2025, 1–18(2025). https://doi.org/10.1007/S42247-025-01175-9

Demirtaş, G., Balki, M. K. and Sayin, C., Effects of a CRDI Engine Running on Biodiesel, n-Octanol and Nanoparticle Blended Nanofuel on Performance, Emissions and Combustion, *Arab J. Sci. Eng*., 49, 2565–2580(2024). https://doi.org/10.1007/s13369-023-08266-x

Gadhave, S., Kolhe, A., Urade, A., Kulkarni, P. D., Jaiswal, N., Sonawane, C. R., Pandey, A., Singh, S., Varshaney, D. and Chan, C. K., Exploring the Effects of the Design of Experiments Technique on the Biodiesel Production from Tung Oil, *Eng. Technol. Appl. Sci. Res.,* 15(4), 24396–24401(2025). https://doi.org/10.48084/etasr.11149

Hariram, V., Ramanathan, V., John, P. K. A., Jeffrey, J. A., Paul, R. C., Manigandan, A., Selvakumar, R. and Balaji, D., Influence of TiO_2 Nanoparticles on Engine Parameters at Varied Compression Ratio of CI Engine Fuelled with Biodiesel, *J. Environ. Nanotechnol.,* 14(2), 58–68(2025). https://doi.org/10.13074/jent.2025.06.2511378

Janaki, P., Raviteja, S., Deepthi, S., Kumar, P. A., Prasad, C. D. and Amiti, B. R., Evaluation of Dielectric Properties of Peanut Oil Biodiesel Mixed with Nano-additives, *J. Environ. Nanotechnol*., 13(1), 111–116(2024). https://doi.org/10.13074/jent.2024.03.241514

Jayabal, R., Environmental impact of adding hybrid nanoparticles and hydrogen to the algae biodiesel-diesel blend on engine emissions, *Process Safe. Environ. Protect.,* 198, 107102(2025). https://doi.org/10.1016/j.psep.2025.107102

Jayabal, R. and Rajkumar, R., Environmental Impact of Waste Peel Biodiesel–Butylated Hydroxytoluene Nanoparticle Blends on Diesel Engine Emissions, *Energy Sci. Eng.,* 13(2), 742–751(2025). https://doi.org/10.1002/ese3.2033

Kanwal, H., Anwar, F., Tanvir, A., Abidi, S. H. I. and Mumtaz, M. W., Optimization of trimetallic Cu-Cr-Ca nanoparticle-catalyzed transesterification of amla (Phyllanthus emblica L.) seed oil: analytical characterization and fuel properties of biodiesel, *Rsc Adv.*, 15(18), 13838–13856(2025). https://doi.org/10.1039/d5ra00098j

Kumar, B., Singh, D., Rathore, S. S., Kumar, S., Pathak, P. K. and Sharma, N., Experimental investigation of methyl-ester soybean biodiesel: performance and emission characteristics as an alternative diesel fuel, *J. Therm. Eng.,* 11(6), 1810–1826(2025). https://doi.org/10.14744/thermal.0001048

Lionus, L. G. M., Das, M. C., Jayabal, R., Murugapoopathi, S., D, S. and Mukilarasan, N., Experimental evaluation and neural network modelling of reactivity-controlled compression ignition engine using cashew nut shell oil biodiesel-alumina nanoparticle blend and gasoline injection, *Energy,* 282, 128923(2023). https://doi.org/10.1016/j.energy.2023.128923

Lionus, L. G. M., Murugapoopathi, S., Gavaskar, G., Baligidad, S. M., Jayabal, R., Mukilarasan, M. and Yuvarajan, Y., Optimisation and environmental analysis of waste cashew nut shell oil biodiesel/cerium oxide nanoparticles blends and acetylene fumigation in agricultural diesel engine, *Sustain. Energy Technol. Assess.,* 58, 103375(2023). https://doi.org/10.1016/j.seta.2023.103375

Manalu, J., Salim, I., Himawan, U., Labagai, J. S., Mara, A., Fitriyana, D. F., Anis, S., Dewi, R., Parlaungan Siregar, J. P., Yudiono, H. and Rahman, N. A., Biodiesel Synthesis on Transesterification of Used Cooking Oil Using Modified Clay Catalyst: Temperature Effect Study, *Eng. Lett*., 33(9), 3839–3848(2025).

Nachippan, N. M., Padmanabhan, S., Parthasarathy, M. and Elumalai, P. V., Nano-Alumina Incorporated Mahua Biodiesel and its Impact on Engine Efficiency and Emissions, *Int. J. Vehicle Struc. Syst*., 16(3), 451–456(2024). https://doi.org/10.4273/ijvss.12.1.04

Patel, H. A. and Patel, B. P., Investigation on performance and emission studies of variable compression ratio engine using neem oil biodiesel, *J. Therm. Eng.,* 11(6), 1827–1844(2025). https://doi.org/10.14744/thermal.0001049

Prakash, P., Elumalai, E., Hariharan, H., Josephine, G. R. N. R., Velumayil, R., Asif, M., Chan, C. K., Balambica, B., Sabarish, S., Sanjeevi, B., Reddy, M. V. and Sekar, P., Parameter fine tuning on CRDI engine operated with blends of grape biodiesel and diesel, *Case Stud. Therm. Eng.,* 60, 104701(2024). https://doi.org/10.1016/j.csite.2024.104701

Priya, S. C. and Ranjitha, J., TiO_2 Nano-photocatalyst-driven CO_2 Biofixation and Lipid Accumulation in Brackish Water Cyanobacteria for Sustainable Biodiesel Production, *J. Environ. Nanotechnol*., 14(3), 108–121(2025). https://doi.org/10.13074/jent.2025.09.2521558

Raviteja, S., Sekhar, K. C., Rapeta, S. R., Rao, D. B. and Ushaswini, B., The Combustion and Emission Characteristics of Corn Oil Biodiesel with Titanium Oxide (TiO_2) Nano-additive, *J. Environ. Nanotechnol.,* 13(1), 97–103(2024). https://doi.org/10.13074/jent.2024.03.241512

Sateesh, K. A., Yaliwal, V. S., Murugande, B. K., Banapurmath Nagaraj, N. R., Elumalai, E., Balasubramanian, D., Krupakaran, K. R., Fouad, Y., Soudagar, M. E. M., Le, H. C., Tuan, T. T., Kalam, M. A., Chan, C. K. and Yelamasetti, Y., Effect of nano-particles on the combustion and emission characteristics of a dual fuel engine operated on biodiesel-producer gas combination, *Case Stud. Therm. Eng.*, 64, 105560(2024). https://doi.org/10.1016/j.csite.2024.105560

Vellaiyan, S., Enhancement of combustion performance and emission control in Bauhinia malabarica biodiesel-diesel blends using aluminium oxide nanoparticles and electrostatic precipitators, *Clean. Eng. Technol.,* 26, 100981(2025a). https://doi.org/10.1016/j.clet.2025.100981

Vellaiyan, S., Performance enhancement of a diesel engine using nanoparticle-enriched algae biodiesel-diesel blends with an electrostatic precipitator for nanoparticle emission control, *Energy Convers. Manage.,* 326, 119457(2025b). https://doi.org/10.1016/j.enconman.2024.119457

Yang, Y., Ma, M., Li, L., Chen, S., Liu, Z., Li, F. and Wang, W., Formation characteristics of soot from the combustion of biodiesel-based nanofluid fuel: Influence of non-metallic nanoparticles, *Fuel,* 399, 135484(2025). https://doi.org/10.1016/J.FUEL.2025.135484

Yusuf, A. A., Dandakouta, H., Yahuza, I., Yusuf, D. A., Mujtaba, M. A., El-Shafay, A. S. and Soudagar, M. E. M., Effect of low CeO_2 nanoparticles dosage in biodiesel-blends on combustion parameters and toxic pollutants from common-rail diesel engine, *Atmos. Pollut. Res.,* 13(2), 101305(2022). https://doi.org/10.1016/J.APR.2021.101305